2D numerical modelling of meandering channel formation

Y Xiao[1,*], G Zhou[2] and F S Yang[1]

[1]*National Inland Waterway Regulation Engineering Research Center, Chongqing Jiaotong University, Chongqing, China.*
[2]*Chinese Research Academy of Environmental Sciences, Beijing, China.*
[*]*Corresponding author. e-mail: xymttlove@163.com*

A 2D depth-averaged model for hydrodynamic sediment transport and river morphological adjustment was established. The sediment transport submodel takes into account the influence of non-uniform sediment with bed surface armoring and considers the impact of secondary flow in the direction of bed-load transport and transverse slope of the river bed. The bank erosion submodel incorporates a simple simulation method for updating bank geometry during either degradational or aggradational bed evolution. Comparison of the results obtained by the extended model with experimental and field data, and numerical predictions validate that the proposed model can simulate grain sorting in river bends and duplicate the characteristics of meandering river and its development. The results illustrate that by using its control factors, the improved numerical model can be applied to simulate channel evolution under different scenarios and improve understanding of patterning processes.

1. Introduction

The morphology of natural river channels is determined by the interaction of fluid flow, sediment transport, bank erosion, and bed morphology (Knighton 1984). Investigating the complex mechanism of patterning processes with various control factors has intrigued geomorphologists and river engineers for several decades, and with rapid development of numerical methods in fluid mechanics, computational model has become an important tool for studying the evolution of channel patterns. A common class of high-resolution models of river morphology is two-dimensional (2D) in the horizontal plane (Mosselman 1998). To simulate the bend development and lateral migration of alluvial channels, a 2D numerical model must account for bend flow effects and river bank erosion processes. Subsequent works on helical flow and forces on sediment grains on a transversely sloping bed (e.g., Einstein and Shen 1964; Engelund 1974; Bathurst *et al.* 1979; De Vriend 1977; Odgaard 1981; Kalkwijk and de Vriend 1980) resulted in 2D numerical models. River bank failures are modes of morphological evolution in addition to bed level and bed sediment composition changes. Physical principles have become a major concern over the past two decades. Meander models based on linearized physics-based equations (Ikeda *et al.* 1981; Johannesson and Parker 1989; Zolezzi and Seminara 2001; Crosato 2008) and 2D non-linear physics-based morphological models with erodible banks (Osman and Thorne 1988; Mosselman 1998; Darby *et al.* 2002; Duan 2005) have been established to simulate the channel planform evolution.

Based on advances in numerical modelling and fundamental study on the physical mechanisms of channel evolution, some researchers have suggested using 2D numerical models to study the cause-and-effect relationship between river patterns and various control variables. Meandering rivers (Duan 2005; Duan and Julien 2010; Hyungsuk *et al.*

Keywords. Fluvial process; armored beds; bank erosion; channel evolution; 2D numerical model.

2011) and braided channels (Nicholas and Smith 1999; Xia *et al.* 2003; Schuurman *et al.* 2013) have been replicated in idealized experiment conditions with detailed data of river characteristics.

The objective of this study is to improve a 2D depth-averaged model for the simulation of channel morphological changes over a short time scale. The original 2D numerical model is upgraded herein to incorporate the effects of non-uniform sediment with armored beds and secondary flow on its transportation in the sediment transport model. A simple method considering the influence of river bend was adopted to establish the non-cohesive bank erosion model. The performance of the model was assessed using a combination of experimental and field data to evaluate the modification of the model. The improved 2D numerical model was applied to a 180° bend with a constant radius under unsteady flow conditions, while the bank erosion model was tested with the physical modelling of the meandering channels by Friedkin, and then applied to the middle reach of Yangtze River. The results implicate that the proposed 2D numerical model is not only capable of simulating the development of single-thread meandering river, but also the evolution of the chute-off and the transformation between different channel patterns with different control factors.

2. Hydrodynamic model

The hydrodynamic portion of the original 2D numerical model is fully described in Wang *et al.* (2010a) and summarized here. It solves the Reynolds-averaged Navier–Stokes equations of mass and momentum conservation in an orthogonal curvilinear grid system:

$$\frac{\partial Z}{\partial t}+\frac{1}{J}\left[\frac{\partial(h_2 q)}{\partial \xi}+\frac{\partial(h_1 p)}{\partial \eta}\right]=0$$

$$\frac{\partial q}{\partial t}+\beta\left(\frac{1}{J}\frac{\partial\left(h_2 qU\right)}{\partial \xi}+\frac{1}{J}\frac{\partial\left(h_1 pU\right)}{\partial \eta}-\frac{pV}{J}\frac{\partial h_2}{\partial \xi}+\frac{qV}{J}\frac{\partial h_1}{\partial \eta}\right)-fp+\frac{gH}{h_1}\frac{\partial Z}{\partial \xi}+\frac{qg\left|\overline{q}\right|}{(CH)^2}$$
$$=\frac{v_e H}{h_1}\frac{\partial E}{\partial \xi}-\frac{v_e H}{h_1}\frac{\partial F}{\partial \eta}+\frac{1}{J}\frac{\partial\left(h_2 D_{11}\right)}{\partial \xi}+\frac{1}{J}\frac{\partial\left(h_{11} D_{12}\right)}{\partial \eta}+\frac{1}{J}\frac{\partial h_1}{\partial \xi}D_{12}-\frac{1}{J}\frac{\partial h_2}{\partial \xi}D_{22} \quad (1)$$

$$\frac{\partial p}{\partial t}+\beta\left(\frac{1}{J}\frac{\partial\left(h_2 qV\right)}{\partial \xi}+\frac{1}{J}\frac{\partial\left(h_1 pV\right)}{\partial \eta}+\frac{pU}{J}\frac{\partial h_2}{\partial \xi}-\frac{qU}{J}\frac{\partial h_1}{\partial \eta}\right)+fp+\frac{gH}{h_2}\frac{\partial Z}{\partial \eta}+\frac{pg\left|\overline{q}\right|}{(CH)^2}$$
$$=\frac{v_e H}{h_2}\frac{\partial E}{\partial \eta}+\frac{v_e H}{h_1}\frac{\partial F}{\partial \xi}+\frac{1}{J}\frac{\partial\left(h_2 D_{12}\right)}{\partial \xi}+\frac{1}{J}\frac{\partial\left(h_1 D_{22}\right)}{\partial \eta}-\frac{1}{J}\frac{\partial h_1}{\partial \eta}D_{11}+\frac{1}{J}\frac{\partial h_2}{\partial \xi}D_{12}$$

$$E=\frac{1}{J}\left[\frac{\partial\left(h_2 U\right)}{\partial \xi}+\frac{\partial\left(h_1 V\right)}{\partial \eta}\right],$$

$$F=\frac{1}{J}\left[\frac{\partial\left(h_2 V\right)}{\partial \xi}-\frac{\partial\left(h_1 U\right)}{\partial \eta}\right]$$

$$h_1=\sqrt{\left(\frac{\partial x}{\partial \xi}\right)^2+\left(\frac{\partial y}{\partial \xi}\right)^2},$$

$$h_2=\sqrt{\left(\frac{\partial x}{\partial \eta}\right)^2+\left(\frac{\partial y}{\partial \eta}\right)^2}$$

where ξ and η are the orthogonal curvilinear coordinates; h_1 and h_2 are the Lamé coefficients; J is the Jacobian of the transformation $J=h_1 h_2$; U and V are the depth-averaged velocity components in the ξ and η directions; the unit discharge vector is $\overline{q}=(q,\,p)=(UH,\,VH)$; Z is the water level relative to the reference plane; H is the total water depth; β is the correction factor for the non-uniformity of the vertical velocity; f is the Coriolis parameter; g is the gravitational acceleration; C is the Chezy coefficient; v_e is the depth mean effective vortex viscosity; and D_{11}, D_{12}, D_{21}, D_{22} are the depth-averaged dispersion stress terms. The effect of the secondary currents is considered by the method of Lien *et al.* (1999):

$$D_{11}=-\int_{z_b}^{z_s}(u-U)^2 dz,\ D_{22}$$
$$=-\int_{z_b}^{z_s}(v-V)^2 dz,\ D_{12}$$
$$=D_{21}=-\int_{z_b}^{z_s}(u-U)(v-V)^2 dz \quad (2)$$

where u and v are the time-averaged velocity components, and z_s, z_b are the dependent water levels of the water surface and channel bed, respectively.

The numerical solution of this model is based on a finite difference method in the orthogonal curvilinear coordinate system. The finite difference equations corresponding to the differential equations are expressed in an alternating direction implicit form. All the discretization procedures are based on a second-order central difference scheme, except for the time differentials of water level in

the continuity equation, which use a forward difference scheme. For the advective accelerations in the momentum equations, a combination of the first-order upwind scheme and second-order central difference can be used (Falconer 1986).

3. Sediment transport model

A description of the suspended sediment model can be found in Wang *et al.* (2010a). In this study, the bed load transport model is upgraded to incorporate the effects of secondary flow and armored beds based on the original 2D numerical model.

3.1 *Influence of bed slope and secondary flow*

The direction of the sediment transport owing to the effect of bed slope can be expressed as (Koch and Flokstra 1981):

$$\tan\alpha = \frac{\sin\delta - (1/f(\theta))\,(\partial\eta_b/\partial n)}{\cos\delta - (1/f(\theta))\,(\partial\eta_b/\partial s)} \tag{3}$$

where δ is the direction of bed shear stress; $\partial\eta_b/\partial n$ and $\partial\eta_b/\partial s$ are the slopes along the ξ and η directions respectively; $f(\theta)$ is a weight function to reflect the effect of the transverse bed slope; and θ is the shields parameter. Several studies have proposed formulations for $f(\theta)$ (Zimmerman and Kennedy 1978; Ikeda *et al.* 1987; Kovacs and Parker 1994), but in this study, we adopt the formula by Talmon *et al.* (1995):

$$f(\theta) = 9\left(\frac{D_{50}}{H}\right)^{0.3}\sqrt{\theta} \tag{4}$$

where D_{50} is the median diameter of the bed material.

Because the direction of the bed shear stress deviates from the direction of the mean flow velocity due to the influence of secondary flow in the meander bend, it is necessary to correlate the sediment transport direction. The effect was introduced by De Vriend (1977) as:

$$\delta = \tan^{-1}\left(\frac{v}{u}\right) - \tan^{-1}\left(\frac{A}{r_s}h\right) \tag{5}$$

where

$$A = \frac{2}{\kappa^2}\left[1 - \frac{n\sqrt{g}}{\kappa h^{1/6}}\right];$$

k is the von Karman constant; n is the Manning's roughness coefficient; and r_s is the local radius of curvature of the streamline calculated from the body-fitted coordinate system by:

$$\frac{1}{r_s} = \frac{1}{\sqrt{(u^2+v^2)^3}} \times \begin{bmatrix} u^2\left(\xi_x\frac{\partial v}{\partial\xi} + \eta_x\frac{\partial v}{\partial\eta}\right) + uv\left(\xi_x\frac{\partial v}{\partial\xi} + \eta_y\frac{\partial v}{\partial\eta}\right) \\ -uv\left(\xi_x\frac{\partial u}{\partial\xi} + \eta_y\frac{\partial u}{\partial\eta}\right) - v^2\left(\xi_y\frac{\partial u}{\partial\xi} + \eta_y\frac{\partial u}{\partial\eta}\right) \end{bmatrix} \tag{6}$$

3.2 *Influence of bed surface armoring*

The total sediment transport of the non-uniform bed material is given by the Engelund–Hansen formula (Kassem and Chaudhry 2005):

$$q_{b*} = 0.05\left(u^2+v^2\right)\sqrt{\frac{D_{50}}{g\,(s-1)}}\left[\frac{\tau_0}{(\gamma_s-\gamma)\,D_{50}}\right]^{3/2}, \tag{7}$$

$$\tau_0 = \gamma\left(\frac{u^2+v^2}{C^2}\right),\ C = 18\log\left(\frac{12h}{3D_{90}}\right). \tag{8}$$

The sediment transport of grain size k can be written as:

$$q_{b*k} = q_{b*}\frac{F_k D_k^{3/2}}{D_{50}^{3/2}}, \tag{9}$$

where q_{b*} is the volumetric sediment transport per unit length; τ_0 is the bed shear stress; q_{b*k} is the volumetric sediment transport per unit length for particle size k; D_k is the representative sediment size of kth fraction; F_k is the proportion of the size fraction k in the mixture of bed materials; s is the specific gravity of sediment; γ_s is specific weight of sediment; and γ is the specific weight of fluid.

Bed armoring is a process in which large-sized particles form an armored top coat on the channel bed, reducing further degradation. Karim and Holly (1986) used a 1D method for bed armoring in alluvial channels to simulate the bed degradation in the Missouri River downstream of Gavins Point Dam and obtained reasonable results with the observed bed characteristics. In this study, we extended the approach into the 2D domain and updated the non-uniform sediment transport at the computational node (i, j):

$$q_{a*bki,j} = q_{b*ki,j}(1 - C_1 A_{fki,j}(t)) \tag{10}$$

in which $q_{a*bki,j}$ and $q_{b*ki,j}$ denote sediment transport per unit width, with and without armoring for group k, respectively; C_1 is between 0 and ~1 (Karim and Holly 1986), which is utilized to correct the surface area covered with the armoring

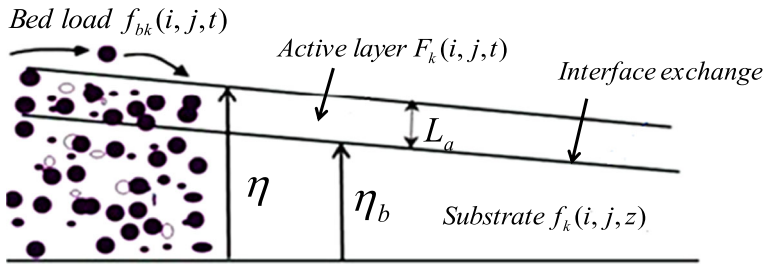

Figure 1. Definition diagram of the active layer concept (Garcia 2008).

particles and $A_{fki,j}(t)$ is a coverage factor of group k in the form:

$$A_{fki,j}(t) = C_A(1-\lambda)d_{si,j}(t)\frac{F_k}{D_k}, \quad D_k \geq l_{i,j}$$
$$A_{fki,j}(t) = 0, \quad D_k < l_{i,j} \tag{11}$$

where λ is porosity; the value of C_A is 1.9 (Karim and Holly 1986); $d_{si,j}(t)$ is the cumulative degradation depth at time t; and $l_{i,j}$ is the index for the smallest sediment size that becomes part of the armor layer and can be obtained by the shields' criterion with the method of Van Rijn (1993) as follows:

$$\begin{cases} \theta_{ck} = 0.24(D_{*k})^{-1} & D_{*k} \leq 4 \\ \theta_{ck} = 0.14(D_{*k})^{-0.64} & 4 < D_{*k} \leq 10 \\ \theta_{ck} = 0.04(D_{*k})^{-0.10} & 10 < D_{*k} \leq 20 \\ \theta_{ck} = 0.013(D_{*k})^{-0.29} & 20 < D_{*k} \leq 150 \\ \theta_{ck} = 0.055 & 150 < D_{*k} \end{cases}$$
$$\text{if } D_k > \frac{\tau_{bi,j}}{\theta_{ck}(s-1)\gamma} \quad l_{i,j} = \min(D_k \cdots D_N), \tag{12}$$

where $\tau_{bi,j}$ denotes the bed shear stress at the computational node (i,j); N is the total number of size fraction; and D_{*k} is the dimensionless particle parameter of group k.

3.3 *Numerical method for hydraulic sorting of bed sediments*

Consider a bed in which the active layer of thickness L_a is defined so that all bed fluctuations are assumed to be concentrated in the well-mixed layer of finite thickness (figure 1) (Garcia 2008). The fractions F_k of bed materials in the active layer can be denoted as $F_k(i,j,t)$, assuming that the fractions have been averaged over fluctuations and the surface layer is perfectly mixed by the fluctuations. The size fractions in the substrate are denoted as $F_{sk}(i,j,z)$ and cannot be functions of t because they are assumed to be below the level of bed fluctuations.

According to the sediment mass conservation for the bed surface, the basic equation for the variation of bed material composition in the active layer without sediment suspension generalizes to (Garcia 2008):

$$(1-\lambda)\left[f_{Ik}\frac{\partial \eta}{\partial t} + \frac{\partial}{\partial t}(L_a F_k)\right] = -\frac{\partial q_{bk\eta}}{\partial \eta} - \frac{\partial q_{bk\xi}}{\partial \xi} \tag{13}$$

where f_{Ik} describes the mean size distribution of the sediment exchanged between the surface layer and the substrate as the bed aggrades or degrades; and, $q_{bk\xi}$ and $q_{bk\eta}$ are the rates of bed load transport in the ξ and η directions.

In this study, we assumed that the active surface layer remains at a constant thickness L_a. The grain size distribution for the surface layer distribution was recalculated according to the volume of sediment entering or leaving the cell at each time step (figure 2).

During aggradation $\Delta z_b > 0$, the new surface layer fraction of group k is:

$$F_k = \frac{\left(\frac{\partial q_{bk\eta}}{\partial \eta} + \frac{\partial q_{bk\zeta}}{\partial \zeta}\right)\cdot A_e + A_e \cdot (1-\lambda)(L_a - \Delta z_b)\cdot F_k}{L_a A_e \cdot (1-\lambda)},$$
$$0 < \Delta z_b < L_a \tag{14}$$

$$F_k = f_{bk}(i,j,t) = \frac{\left(\frac{\partial q_{bk\eta}}{\partial \eta} + \frac{\partial q_{bk\zeta}}{\partial \zeta}\right)\cdot A_e}{\Delta z_b \cdot A_e},$$
$$\Delta z_b > L_a \tag{15}$$

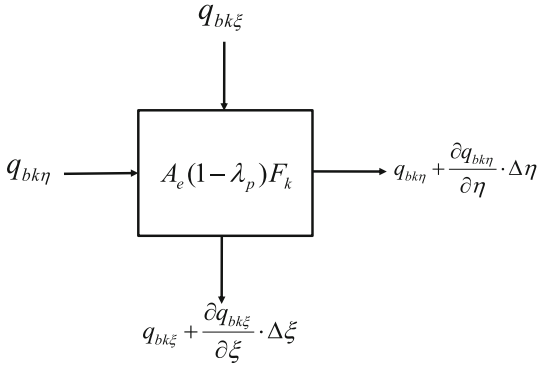

Figure 2. Diagram to illustrate sediment flux entering and leaving the cell with an area, A_E.

where A_e denotes the area of the computational cell.

During degradation $\Delta z_b < 0$, the sediment leaves the cell and the surface layer mixes with the substrate to maintain a constant L_a. The new surface layer fraction F_k is therefore:

$$F_k = \frac{[\Delta z_b F_{sk} + (L_a + \Delta z_b)F_k] \cdot A_e \cdot (1-\lambda)}{L_a A_e \cdot (1-\lambda)}, \quad -L_a < \Delta z_b < 0 \tag{16}$$

$$F_k = F_{sk}(i,j,z), \quad \Delta z_b < -L_a. \tag{17}$$

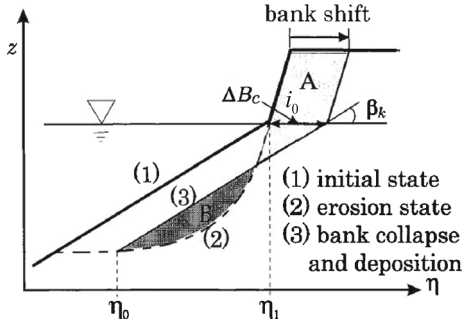

Figure 3. The model of bank failure by Hasegawa (1981).

3.4 *Computation of bed deformation*

The bed deformation can be calculated from the overall mass balance equation of the sediment as follows (Garcia 2008):

$$\sum_{k=1}^{N} \frac{1}{1-\lambda} \cdot \frac{\partial Z_k}{\partial t} + \sum_{k=1}^{N} \frac{1}{J}\left[\frac{\partial h_2 q_{bk\xi}}{\partial \xi} + \frac{\partial h_1 q_{bk\eta}}{\partial \eta}\right] + \sum_{k=1}^{N} \alpha_k \omega_k (S_k - S_{*k}) = 0, \tag{18}$$

where Z_k is the thickness of the sediment layer; α_k is the saturation recovery coefficient for sediment fraction k; ω_k is the fall velocity for sediment fraction k; and S_k and S_{*k} are the suspended-load concentration and transport capacity of kth sediment fraction, respectively.

4. Numerical algorithm of non-cohesive bank erosion

The influence of bank geometry and river bend was considered in the non-cohesive bank erosion model in this study. The computational grid remains stationary in the calculation, which ensures that the horizontal positions of all the compute nodes remain unchanged but allows the bed elevation and wet type to be changed. The wet type in the calculation domain can be divided into water boundary grid cell, marked '1', and dry boundary grid cell, marked '0', during the simulation process.

We adopted an intermittent bank erosion model proposed by Hasegawa (1981), who conducted experiments on the bank erosion process and found that bank profiles are similar after bank collapse, forming slopes with the repose angle of the sediment. In the simplified model for non-cohesive bank failure (figure 3), line (1) is the initial shape of the side bank, and the side bank profile changes to line (2) after bed scouring. Line (3) shows the bank profile after the upper part of bank (A) collapses and deposits on the bed. The slope angles of lines (1) and (3), β_k, are regarded as the angle of repose for the bank materials, and i_o is the bank angle above the water surface.

4.1 *Influence of bank geometry for meander bends*

Bank erosion processes involve the complex interaction of flow field, bank material, and bank geometry. The retreat length ΔB_c depends on bank size, shape and materials, determined by the bank stability (Darby and Thorne 1996). To simplify the numerical procedures, we assumed that the lateral erosion distance ΔB_c follows Osman and Thorne (1988):

$$\Delta B_c = C_l \Delta t (\tau - \tau_c) e^{-0.13\tau_c} / \gamma_{bk} \tag{19}$$

where C_l is erodibility coefficient, related to bank soil properties; $\Delta t\,(s)$ is the time increment; τ_c is the critical shear stress for the bank material; γ_{bk} is the specific weight of bank soil; and τ is the flow shear stress acting on the banks in the near bank zone.

According to pioneering works on the effect of secondary flow in meander bends, the distribution of bed shear stress agrees with the longitudinal velocity (Varshney 1975), and the bed shear stress can be obtained by:

$$\tau = (u/V)^2 \tau_0 = \gamma u^2 / C^2. \tag{20}$$

Owing to the influence of longitudinal and transverse bed-slope, the gravity component may result in distinct mechanical characteristics between bank and bed material. In practice, the bank always has a slope so that the incipient motion condition would be different from the condition on a horizontal bottom, with the critical shear stress expressed following Van Rijn (1989):

$$\tau_c = k_1 k_2 \tau_* \tag{21}$$

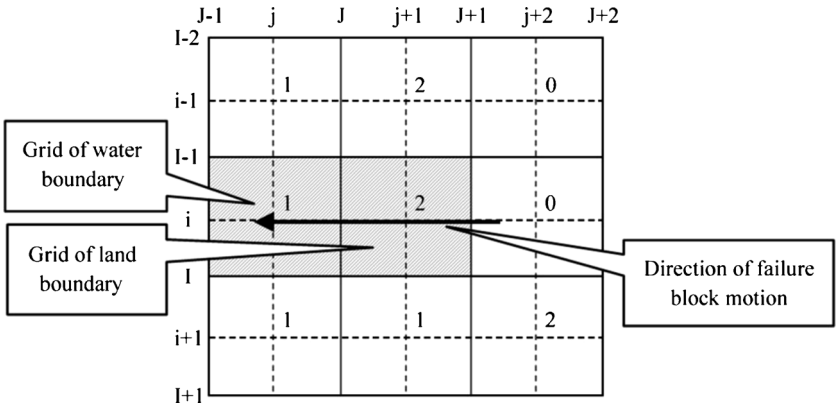

Figure 4. Classification of the bank failure grid.

where τ_* is the critical mobility parameter on a horizontal bottom and the coefficient k_1 is defined as:

$$k_1 = \begin{cases} \sin(\varphi + \beta_1)/\sin\varphi, & \beta_1 \geq 0 \\ \sin(\varphi - \beta_1)/\sin\varphi, & \beta_1 < 0 \end{cases}$$
$$k_2 = \cos\gamma_1 \left(1 - \tan^2\gamma_1/\tan\varphi\right)^{1/2} \qquad (22)$$

where β_1 is the longitudinal bed-slope angle; γ_1 is the lateral bed-slope angle and φ is the angle of response. More details on the expressions of k_1 and k_2 can be found in Julien and Anthony (2002).

4.2 *The numerical algorithm for non-cohesive bank erosion*

Based on the common wet type, we add a new group '2' as the land boundary grid cell, which has at least one side next to a water boundary grid cell marked '1' (figure 4), has a higher bottom elevation at the center of the cell than the water stage, and is excluded in the computation for flow and sediment transport. We assumed that only one side of the land boundary grid cell $(i, j{+}1)$ can fail when the shear stress exceeds the critical shear stress (figure 4); the shear stress at the two common sides between the three grid cells are then compared, and whichever has the largest shear stress fails. The grid cell marked '2' should be included in the solution process for water flow and sediment transport after its bank fails and becomes 'wet' (Wang *et al.* 2010a).

Because the horizontal position at all computational nodes remains unchanged, a memory array was established to handle alterations of dry and wet nodes. The array includes the location of boundary grid, bed elevation of the boundary grid, and the cumulative lateral erosion distance ΔB. The parameters Δp and ΔL should be used to determine the modification of the memory array:

$$\Delta p = \frac{h_f}{\tan i_0} \quad \Delta L = \frac{H}{\tan\beta_k}. \qquad (23)$$

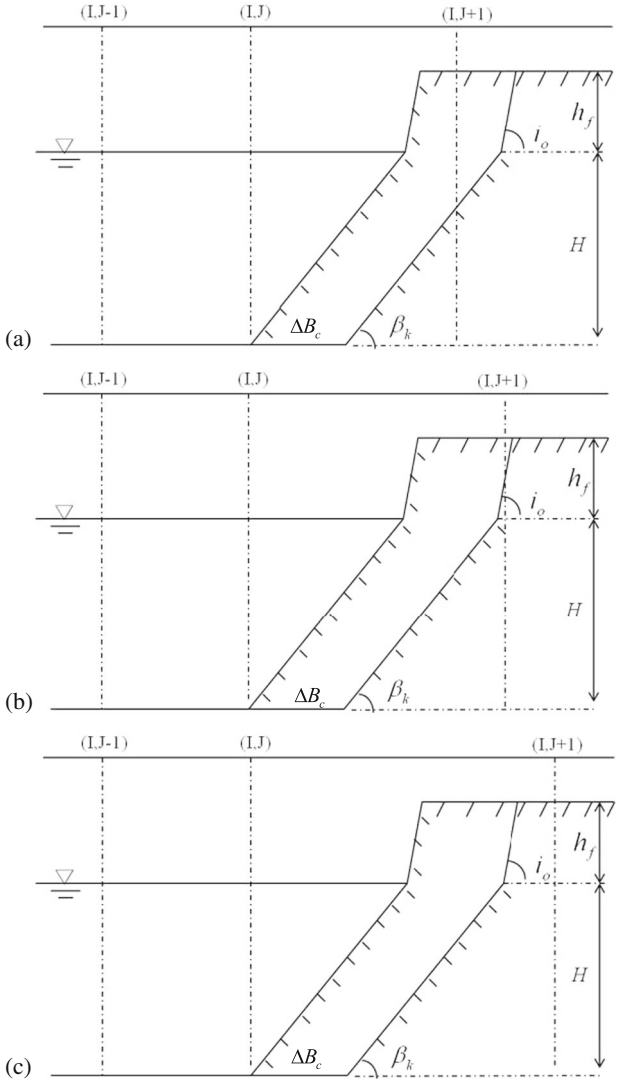

Figure 5. Calculation method for bank erosion.

If $\Delta B + \Delta L > x(i, j+1) - x(i, j)$, then the land boundary node $(i, j+1)$ should be included in the solution process for water flow and sediment transport. The wet type of node $(i, j+1)$ becomes '1', and the bed elevation is adjusted with geometrical

relationships (figure 5a). The memory array should update the information for the new boundary grid and reset $\Delta B = 0$ after the bank failure.

If $\Delta B + \Delta L \le x(i,j) - x(i-1,j) \le \Delta B + \Delta L + \Delta p$, the bed elevation at land boundary node $(i, j+1)$ is adjusted with geometrical relationship while the wet type remains '2' (figure 5b). The memory array should record the modified bed elevation and the cumulative lateral erosion distance ΔB for the next computational time step.

If $x(i,j+1) - x(i,j) > \Delta B + \Delta L + \Delta p$, both the bed elevation and wet type at the land boundary

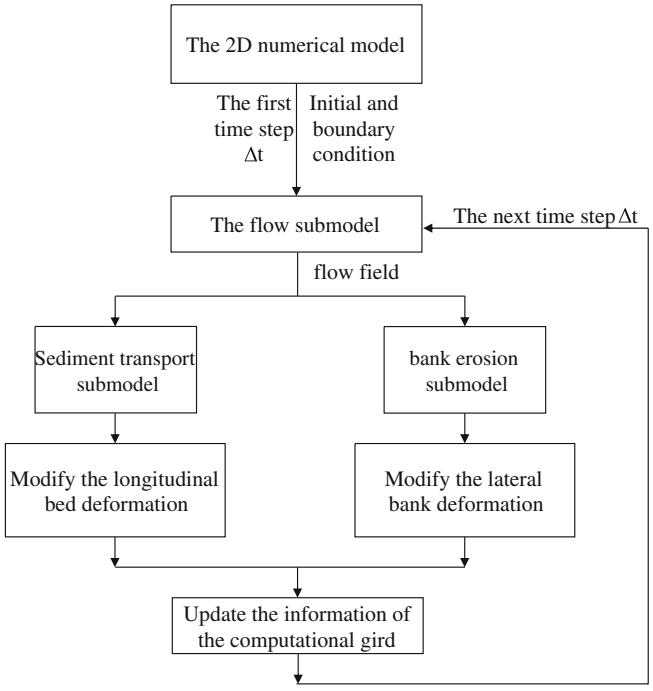

Figure 6. Solution procedure for the 2D numerical model.

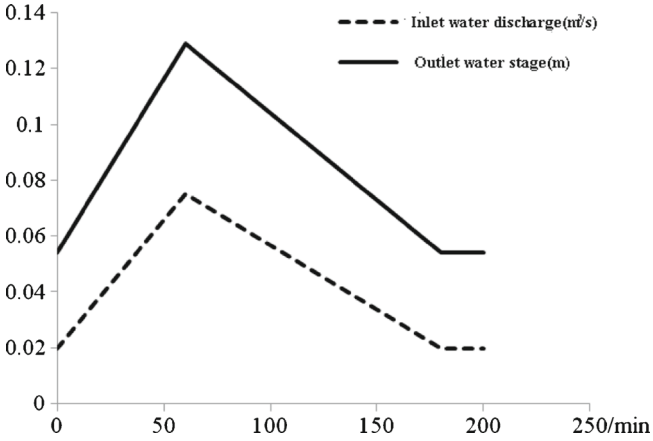

Figure 7. The simulated condition.

Table 1. *The fraction of sediment in this simulation.*

No.	1	2	3	4	5	6
Size (mm)	0.5	0.75	1.25	2	3	5
Proportion	0.25	0.25	0.1	0.15	0.15	0.1

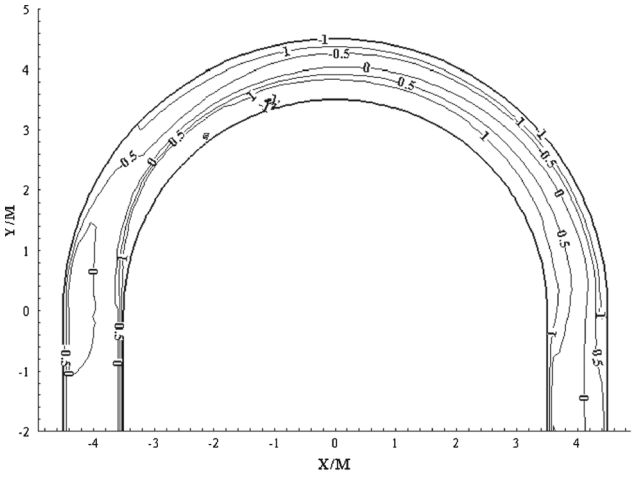

(a) Bed deformation without armoring effect

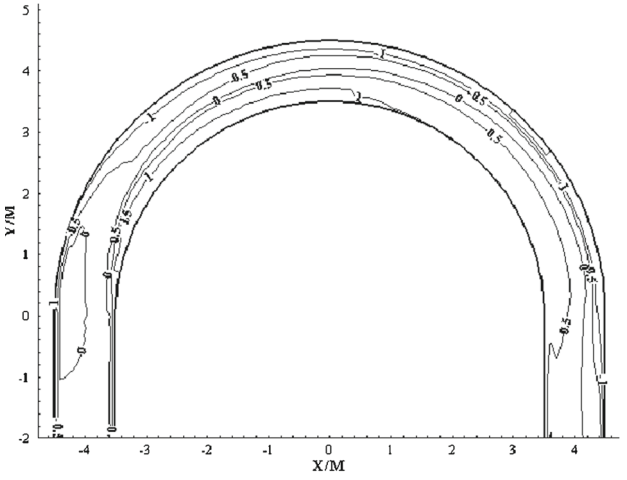

(b) Bed deformation with armoring effect

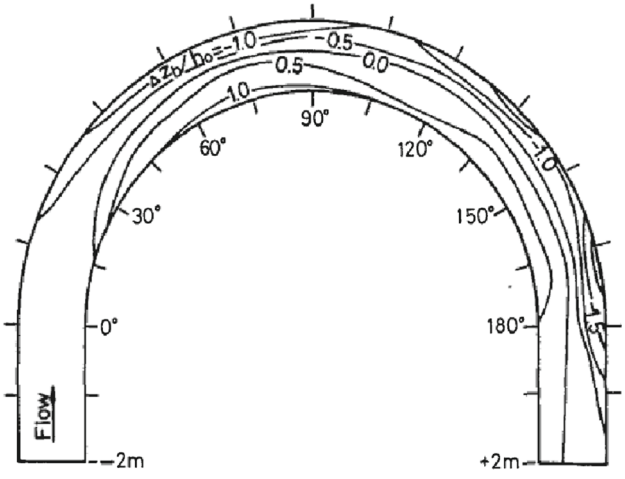

(c) The bed deformation of measured data

Figure 8. The simulated and measured contours of bed deformation (z_b/h).

node $(i, j+1)$ remains unchanged (figure 5c), and the lateral erosion distance ΔB should be included in the subsequent time intervals with the memory array.

5. Solution procedures for the 2D numerical model

The 2D depth-averaged model includes three submodels: flow, sediment transport, and bank erosion. The corresponding computational procedures (figure 6) consist of six steps:

(1) Input the initial and boundary conditions, including the initial bed topography, flow and sediment conditions.
(2) Compute the flow field while keeping the bed and bank configuration fixed by the 2D flow submodel.
(3) Simulate the process of lateral erosion using the bank erosion model with the flow field.

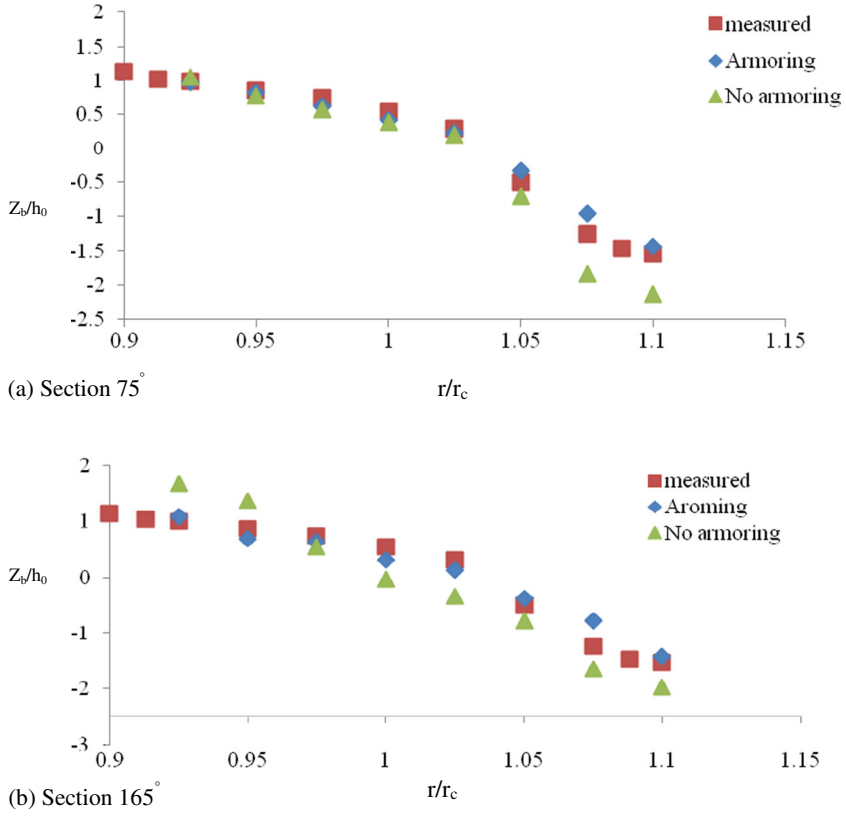

Figure 9. Measured and computed transverse bed profiles.

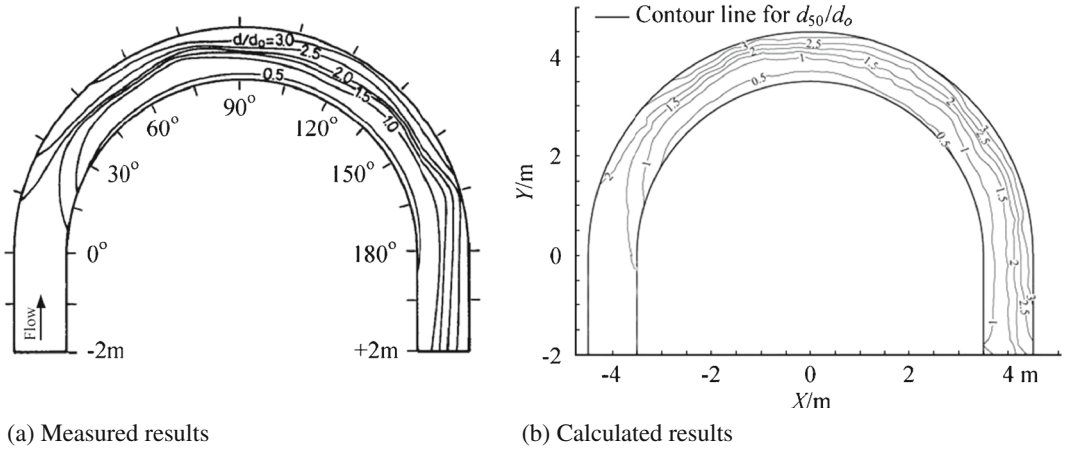

Figure 10. Computed and measured contours of the median sediment size.

(4) Compute the sediment rate of kth group and the bed deformation by the sediment transport submodel.
(5) Modify the bed elevation according to the changes of longitudinal and lateral bed deformations.
(6) Update the surface layer fraction with equations (14–16) and the cumulative degradation depth $d_{si,j}(t)$ to compute the sediment transport equation (10) for the next time step.

By repeating steps (2)–(6), the development of the channel planform in the longitudinal and lateral directions can be obtained.

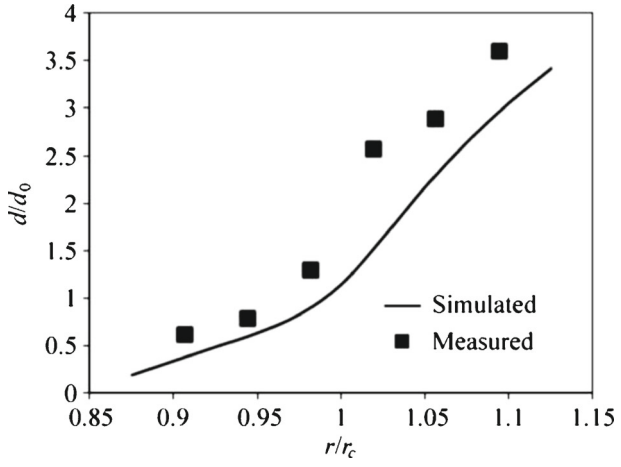

Figure 11. Measured and computed transverse variation of sediment size at section 90°.

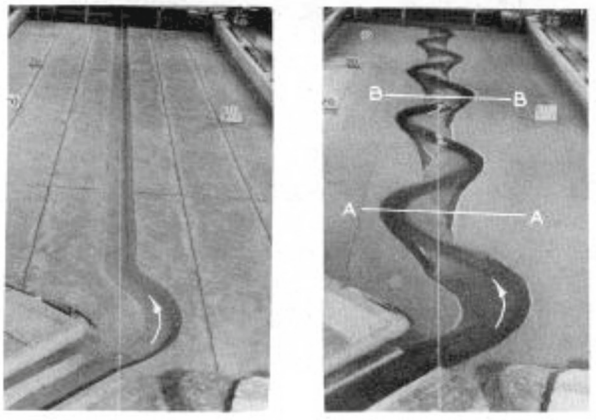

(1) Initial channel (2) The planform after 3 hours

Figure 12. Planform of the physical channel (Friedkin 1945).

6. Verification

6.1 *Yen and Lee's Experiment (1995)*

To investigate the applicability of the sediment transport model presented herein, an experiment of bed deformation in a 180° bend channel (Yen and Lee 1995) was simulated. The bend was connected with a stilling basin, an upstream straight reach of 11.5 m, and a downstream straight reach of the same length. The radius of the channel bend was 4 m, and the cross section was a 1 m-wide rectangle. The initial bed was flat with 0.2% slope. The water discharge and the outlet water level were shown in figure 7. The median grain size of the sediment was 1.0 mm and divided into six groups in computation (table 1). A mesh of 339×11 nodes was applied, no sediment was supplied from upstream, and the thickness of the active layer was 0.2 m during the simulation. The quasi-steady approximation (the bed topography can be decoupled from the flow computation) was used herein.

The bed equilibrium topography was compared between modelled and measured data (figure 8a–c), in which the number of each contour line was defined as the relative bed variations (z_b/h_0) compared with the initial flat bed. The result without armoring effect (figure 8a) indicates a relatively poor comparison with the observed bed levels near the inner bank. The extended model (figure 8b) computed an acceptable result with the measured data (figure 8c); however, the sediment deposition in the point bar (inner bank) and erosion in the outer bank (upstream from the apex of the bend) were underestimated.

A comparison of the transverse bed profiles between measured data and computed data with and without armoring at section 75° and 165° (figure 9a and b) indicated that the maximum

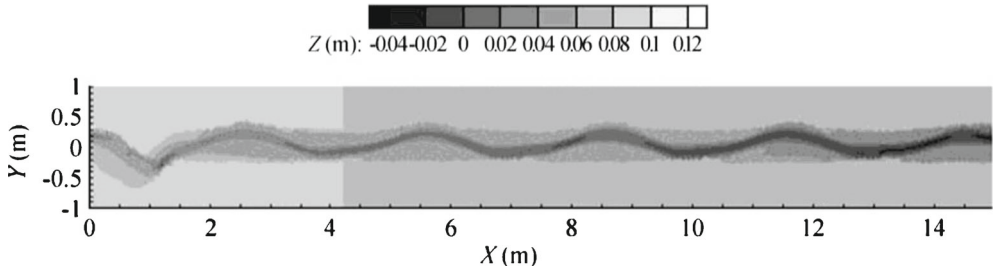

Figure 13. Planform of the simulated channel with original model.

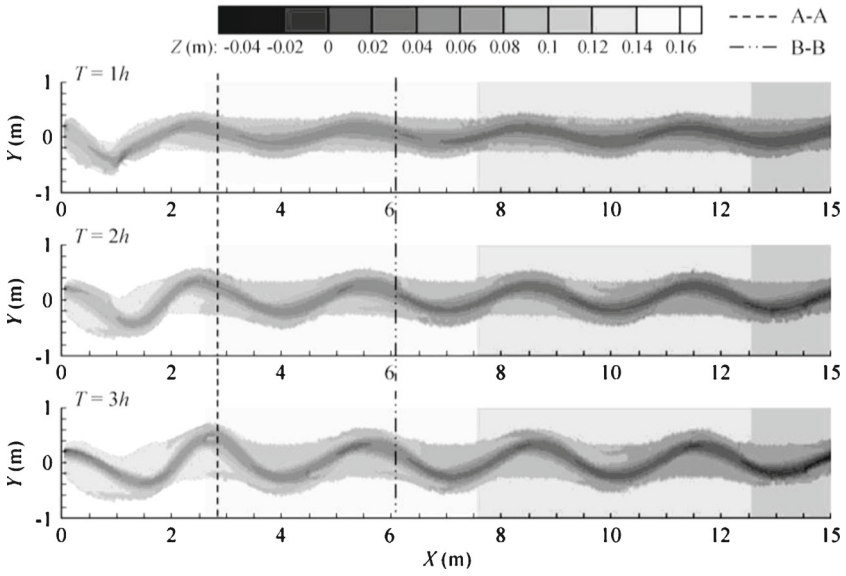

Figure 14. Planform of the simulated channel with the extended model with time.

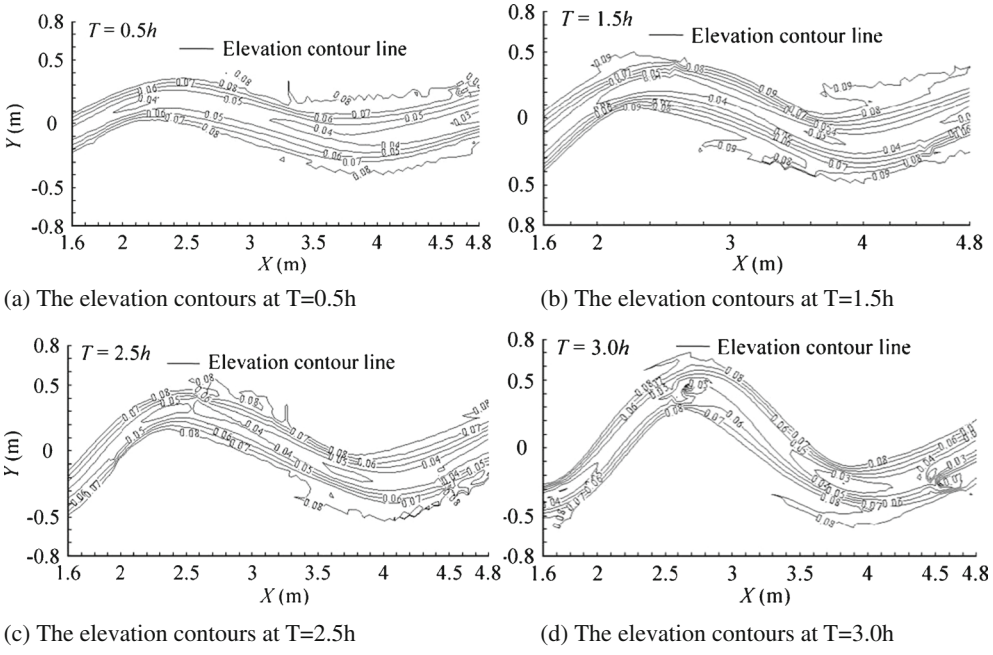

(a) The elevation contours at T=0.5h

(b) The elevation contours at T=1.5h

(c) The elevation contours at T=2.5h

(d) The elevation contours at T=3.0h

Figure 15. The simulated contours of bed deformation for the second river bend with time (numbers in m).

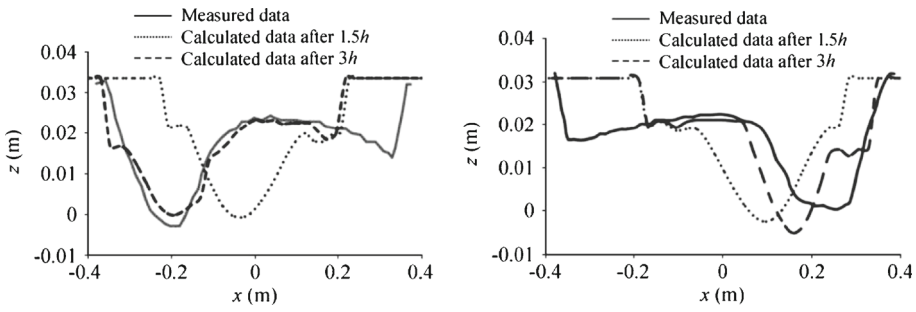

(a) A-A section

(b) B-B section

Figure 16. Comparison of water depth at the A–A and B–B sections.

deposition occurred near the inner bank, and the maximum scour depth took place near the outer bank. Compared with no armoring, the value of maximum scour depth was reduced by bed armoring, which is similar to the finding of Ikeda *et al.* (1987). The computed bed profiles near the centerline of the bend were lower than the measured values at section 75° (figure 9a), possibly due to the uncertainties associated with the secondary flow correction on the bed load redirection. The influence of bed armoring in the inner bank was reduced at section 165° with the development of the channel bend (figure 9b).

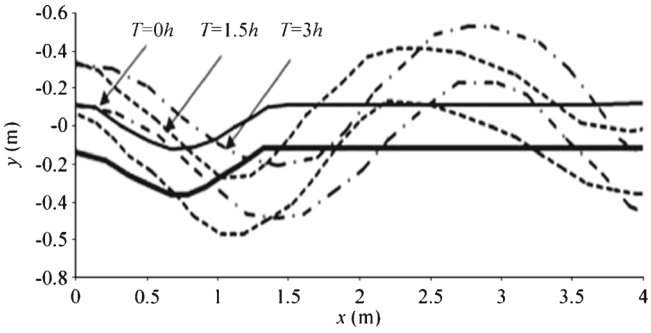

Figure 17. Temporal changes in plan forms of simulated channel.

The contour of d_{50}/d_0 for the bend and the transverse value of d_{50}/d_0 at section 90° (figures 10–11, respectively) shows acceptable agreement with the measured data. The computed result shows that the largest d_{50}/d_0 occurred on the top of the bend near section 90° (figure 10), implying that the high longitudinal velocity and the intensive transverse sorting reduced the hiding effect of the non-uniform sediment in the outer bank region, and the fraction of the fine sediment in this region was relatively less than that in the inner bank (figure 11). The performance of d_{50}/d_0 in the entrance is poor (figure 10) and the same conclusion is obtained in the entrance contours of bed deformation (figure 8b). Further study should be conducted to analyze the influence; however, the improved sediment submodel can be used to simulate the grain sorting in the river bend.

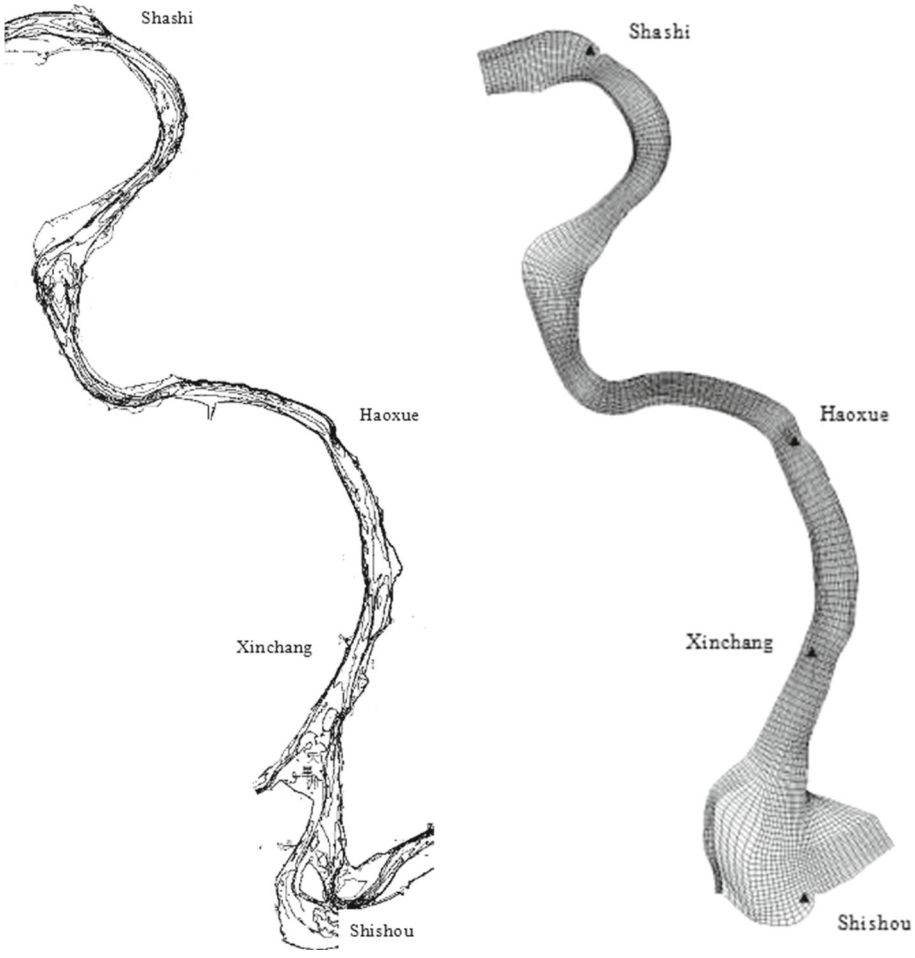

Figure 18. Layout of the field study reach section and its computational mesh.

6.2 *The laboratory study for meandering rivers of Friedkin (1945)*

The work by Friedkin (1945) is now widely regarded as a classic study that has strongly influenced the physical studies (Schumm *et al.* 1987; Braudricka *et al.* 2009; Van Dijk *et al.* 2012). Our goal was to replicate the classical physical modelling of meandering rivers (Friedkin 1945) with the non-cohesive bank erosion submodel and analyze the results to verify the potential of the 2D depth-averaged models for the simulation of the meandering processes.

The physical domain of this river was 14 m long and 4 m wide, and the experimental channel was straight except for an initial bend. The initial cross-section was trapezoidal with a top width of 0.28 m, a bottom width of 0.17 m and a depth of 0.045 m. The initial slope was 0.0075, the media sediment size was 0.45 mm, and sediment was fed at the entrance to prevent the channel from deepening or aggrading just below the entrance. The grid system of 280×80 nodes was generated in the computational domain, with grid spacing of 0.05 m in the ξ and η directions. The water discharge (0.0045 m^3s^{-1}) and tailwater level (0.03 m) were constant. The simulated time interval was Δt = 0.02 s, and the experimental time period was 3 hr.

The bed topography of the laboratory and simulated channel indicate that the development of a series of uniform bends is a result of impingement and deflection from the banks and deposition of sand on the inside of the bend (figures 12–14). The initial bend directed the flow against the bank on the opposite side, the bank was eroded, and sediment was added to the channel. The upstream part of the thalweg began to develop a sinuous path, which extended progressively downstream

Table 2. *The fraction of bed material.*

No.	Group percentage of bed materials									d_{50}(mm)	Year
	0.004	0.008	0.016	0.03	0.062	0.125	0.25	0.5	1		
%	0	0	0	0.1	1.1	13.2	55.3	30	0.3	0.193	2002

Table 3. *The fraction of suspended load being simulated.*

No.	Suspended load group percentage (mm)								d_{50}(mm)	d_{cp} (mm)	Year
	0.004	0.008	0.016	0.031	0.062	0.125	0.25	0.5			
%	30	12.7	13.4	14.6	13.1	8.2	6.5	1.5	0.011	0.036	1992∼2002

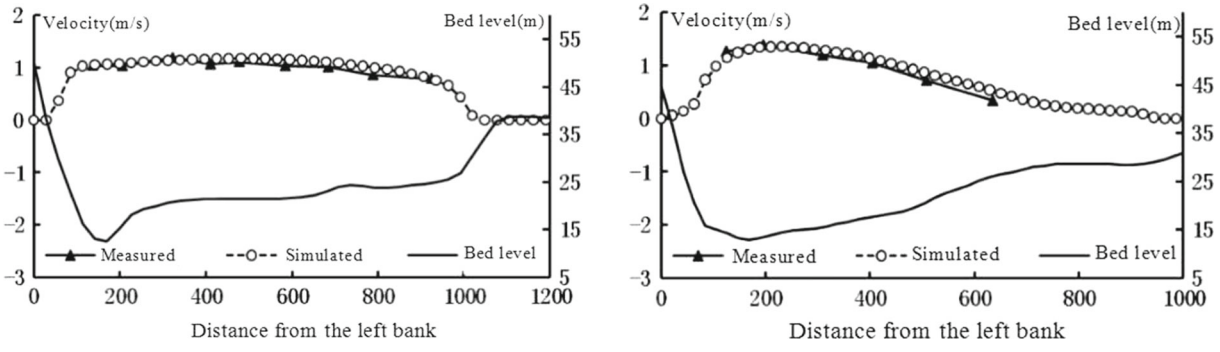

(a) Cross section S1 (b) Cross section S2

Figure 19. Measured and calculated cross-sectional profiles of depth-averaged velocity.

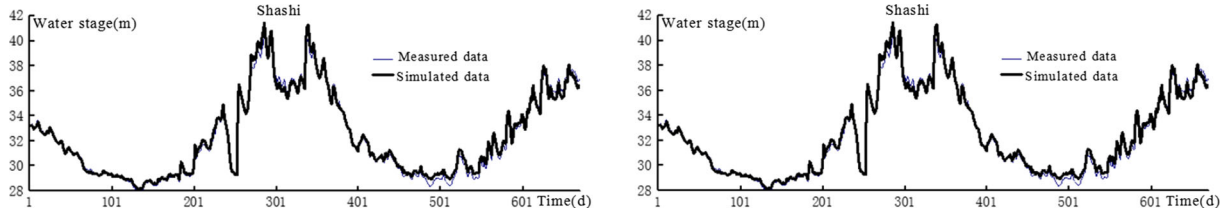

Figure 20. Comparison of the water stages at two control stations.

and directed the flow against the outer banks, causing further erosion on alternate sides of the channel. The calculated channel planform with the original model (figure 13) was not in agreement with the laboratory channel (figure 12); the amplitude of the bend was smaller than the physical model, which contributed to the inaccurate direction of sediment transport in river bend. The extended model can simulate the bed degradation near concave banks and deposition near convex banks and reproduce

Table 4. *Measured and calculated volumes of deposition (+) or scour (−).*

River section	Total distance (km)	Section length (km)	Measured ($10^6 m^3$)	Calculated ($10^6 m^3$)
Taipingkou-Shashi	8.47	8.47	–827.26	–1185.91
Shashi-Haoxue	58.65	50.19	–1705.39	–1730.82
Haoxue-Xinchang	73.62	14.96	–1353.62	–924.21
Xinchang-Shishou	93.38	19.76	–1508.87	–1719.86

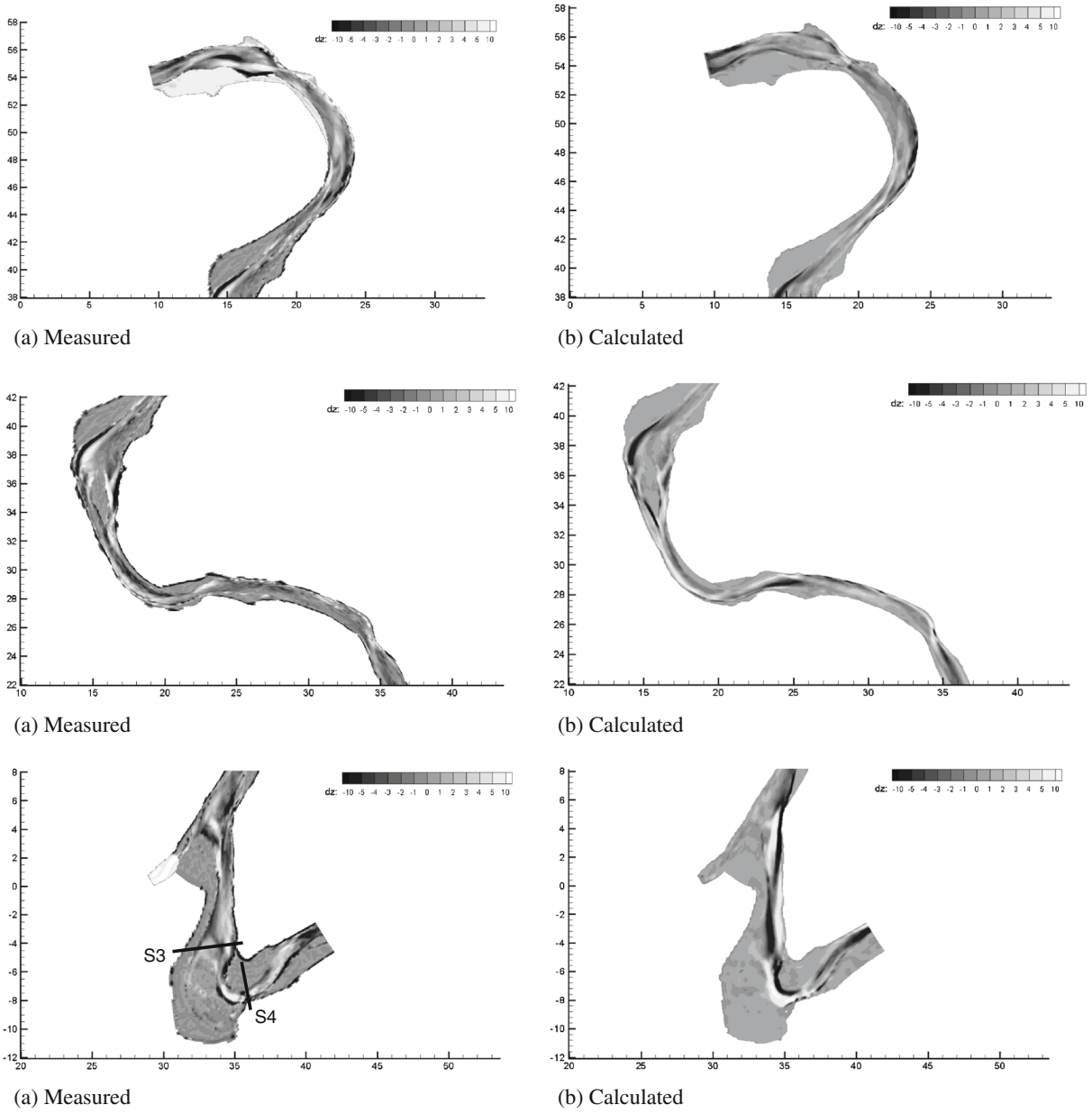

Figure 21. Calculated and measured scour or deposition depths of reach section (m).

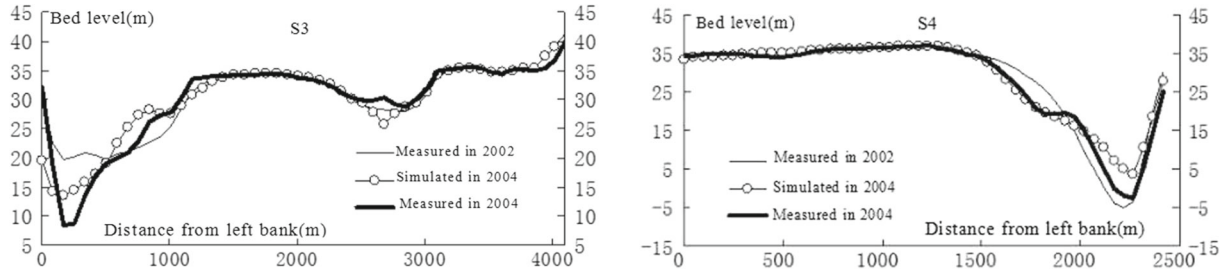

(a) Cross section S3 (b) Cross section S4

Figure 22. Measured and calculated bed deformation at various typical cross-sections.

the bed topography acceptable with the field data (figure 14), implying that the redirection based on secondary flow on bed-load vectors is critical for describing the bed evolution pattern in meandering bends (Abad *et al.* 2008).

The elevation contours of the second meander bend (figure 14) with the extended model (figure 15) show that chutes were formed at the apex with further development of meander bends, a result that compares satisfactorily with the photograph after 3 hours (figure 12). In contrast with the lack of a real-time detailed history of meandering channel evolution in laboratory experiments, the model can record the evolution of the chutes and explicate the formation of river meanders.

A comparison of water depth at the A–A and B–B section at T=3 hr (figure 14) shows that as time progressed, the pattern of the cross sections tended to the deep section at the concave bank after 1.5 hr, bank lines retreated along concave banks and advanced along convex banks, and the deformation of cross section agreed qualitatively with the measured data at T=3 hr (figure 16). Due to the empirical formula for the rate of bank erosion, the lateral extension was smaller than the measured data during the whole simulation time. The temporal change in the planforms (figure 17) shows that once a bend had been initiated, there was a marked tendency for the flow to develop a series of bends downstream.

6.3 *Field evaluation: Case study of middle reach of Yangtze River, China*

The proposed model was applied to a 102 km long, 'S' shaped channel section of the middle Yangtze River from Shashi to Shishou to verify its reliability (figure 18a). An orthogonal curvilinear coordinate system was applied with a total of 600×115 grids in the computational domain and a time interval of t=8 sec (figure 18b). Observed daily water discharge and sediment load at the inlet were used as boundary conditions and bed contour maps dated September 2002 was the initial topography. Calculation of suspended load was divided to eight groups ranging from 0.005 to 1 mm in diameter (table 2). The sediment gradation in bed materials (table 3), transport capacity for various size groups, and river topography were adjusted every 24 hr. The thickness of active layers were L_a = 15 m. A real time period of 2 years was simulated, and calculated results of flow velocity, water stage and morphological changes are compared with the field data.

Comparison of observed and calculated cross-sectional profile of depth averaged stream-wise velocity for various discharges in November 2003 is shown in figure 19. Calculated depth-averaged velocities were consistent with the observed asymmetrical velocity patterns, except for some differences near the bank of the river. Figure 20 shows the comparison of the measured and calculated water stages at two hydrometric stations during September 2002∼July 2004, which indicates good agreements between simulations and measurements.

Table 4 lists the measured and calculated total amount of deposition or scour. It indicates that the largest discrepancy between observed and calculated results was found in the entrance section from Taipingkou-Shashi, possibly due to the uncertainties introduced by the initial and boundary conditions. Figure 21 is a comparison between calculated and measured scour and deposition depths. It can be seen that except the entrance section, the predicted pattern of scour and deposition agrees well with observations if reliable information of bank strength and bed material size can be obtained. A comparison of changes of the bed level at the typical cross sections shows that as time progressed, the pattern of the cross sections tended to the measurements with acceptable ranges of error (figure 22).

7. Conclusion and discussion

Based on the previously developed 2D depth-averaged hydrodynamic model, the model in this

work was upgraded to incorporate the effects of secondary flow and non-uniform sediment with armored beds in the sediment transport model. A simple simulation method considering the influence of river bend was adopted in the non-cohesive bank erosion submodel. Comparison of the results obtained by the extended model with experimental data and numerical predictions validates the proposed model. In the experimental river, the extended model can simulate the chute evolution and the formation of the meandering. In the field case, the model is calibrated to a 102-km long river channel of the middle Yangtze River, China. Predictions are compared with preliminary results of field observations and factors affecting the reliability of the simulated results are discussed. In this 2D numerical model, major parameters or assumptions that may account for the accurate morphological changes of river channel include:

(1) the assumed initial grain size distribution of bed material and the initial thicknesses of active layers of the channel bed;
(2) the grid size, especially near the banks and around the bends; and
(3) the erodibility parameters related to the bank strength.

The results may be helpful to the development of more accurate simulation models in the future. However, the bank erosion submodel is limited to the non-cohesive bank material experiencing planar bank failure and the assumption for the rate of bank failure. The formula for correction on the direction of bed-load transport is empirical; results could improve if a 3D model was applied to simulate the helical flow of the river bend. Further research is needed on the fundamental equation that governs the evolution of alluvial rivers to ensure the availability of the numerical models.

List of symbols

ξ, η:	Orthogonal curvilinear coordinates
h_1, h_2:	Lamé coefficients
J:	Jacobian of the transformation $J = h_1 h_2$
Z:	Water level relative to the reference plane
H:	Total water depth
U, V:	Depth-averaged velocity components in ξ and η directions
β:	Correction factor for the non-uniformity of vertical velocity
f:	Coriolis parameter
g:	Gravitational acceleration
C:	Chezy coefficient
υ_e :	Depth mean effective vortex viscosity
D_{11}, D_{12}, D_{21}, D_{22}:	Depth-averaged dispersion stress terms
z_s, z_b:	Dependent water levels for the water surface and channel bed
δ:	Direction of bed shear stress
$f(\theta)$:	A weight function to reflect the effect of transverse bed slope
θ:	Shields parameter
D_{50}:	Median diameter of bed material
k:	von Karman constant
n:	Manning's roughness coefficient
u, v:	Time-averaged flow velocity components
R_s:	Local radius of curvature of the streamline
τ_0 :	Bed shear stress
$\tau_{bi,j}$:	Bed shear stress at the computational node (i, j)
τ_c:	Critical shear stress for the bank material
τ:	Flow shear stress acting on the banks
τ_*:	Critical mobility parameter on a horizontal bottom
q_{b*}:	Volumetric sediment transport per unit length
q_{b*k}:	Volumetric sediment transport per unit length for particle size k
$q_{a*bki,j}$:	Sediment transport per unit width with armoring for group k
$q_{b*ki,j}$:	Sediment transport per unit width without armoring for group k
$q_{bk\zeta}, q_{bk\eta}$:	Rate of bed load transport in ξ and η directions, respectively
D_k:	Representative sediment size of kth fraction
F_k:	Proportion of the size fraction k in the mixture of bed materials
s:	Specific gravity of sediment
γ_s:	Specific weight of sediment
γ:	Specific weight of fluid
γ_{bk}:	Specific weight of bank soil
C_1:	Parameter to correct the surface area covered with the armoring particles
$A_{fki,j}(t)$:	Coverage factor of group k
$d_{si,j}(t)$:	Cumulative degradation depth at time t
$l_{i,j}$:	Index for the smallest sediment size which becomes part of the armor layer
λ:	Porosity of sediment
N:	Total number of size fraction
D_{*k}:	Dimensionless particle parameter of size group k
f_{Ik}:	Mean size distribution of the sediment
A_e:	Area of computational cell
Z_k:	Thickness of sediment layer
α_k:	Saturation recovery coefficient for size group k
ω_k:	Fall velocity for size group k

S_k, S_{*k}: Suspended-load concentration and transport capacity of kth size group
C_l: Erodibility coefficient
Δt: Time increment
β_1: Longitudinal bed-slope angle
γ_1: Lateral bed-slope angle
ϕ: Angle of response.

Acknowledgements

This research is supported by the National Natural Science Foundation of China (51409027), the Science and Technology Research Foundation of Chongqing Municipal Education Commission (Grant No. KJ1500502).

References

Abad Jorge D, Buscaglia Gustavo C and Garcia Marcelo H 2008 2D stream hydrodynamic, sediment transport and bed morphology model for engineering applications; *Hydrol. Process.* **22** 1443–1359.

Bathurst J C, Thorne C R and Hey R D 1979 Secondary flow and shear stress at river bends; *J. Hydraul. Div.* **105** 1277–1295.

Braudricka C A, Dietrich W E, Leverich G T and Sklar L S 2009 Experimental evidence for the conditions necessary to sustain meandering in coarse-bedded rivers; *PNAS* **106** 16,936–16,941.

Crosato A 2008 Analysis and modelling of river meandering; PhD thesis, Delft University of Technology, The Netherlands, IOS Press, ISBN 978-1-58603-915-8.

De Vriend H J 1977 A mathematical model of steady flow in curved shallow channel; *J. Hydraul. Res.,* Delft, The Netherlands **15(1)** 37–54.

Darby S E and Thorne C R 1996 Numerical simulation of widening and bed deformation of straight sand-bed rivers. I: Model development; *J. Hydraul. Eng.* **122(6)** 184–193.

Darby S E, Alabyan A M and Van de Wiel M J 2002 Numerical simulation of bank erosion and channel migration in meandering rivers; *Water Resour. Res.* **38(11)** 1–21.

Duan Jennifer G 2005 Analytical approach to calculate rate of bank erosion; *J. Hydraul. Eng.* **131(12)** 980–990.

Duan Jennifer G and Julien Pierre Y 2010 Numerical simulation of meandering evolution; *J. Hydrol.* **391** 34–46.

Einstein H A and Shen H W 1964 A study of meandering in straight alluvial channels; *J. Geophys. Res.* **69** 5239–5247.

Engelund F 1974 Flow and bed topography in channel bends; *J. Hydraul. Eng.* **100** 1631–1648.

Falconer R A 1986 Water quality simulation study of a natural harbor; *J. Waterway, Port, Coastal, and Ocean Engineering* **112** 15–34.

Friedkin J 1945 A laboratory study of the meandering of alluvial rivers; US Waterways Experiment station: Vicksburg.

Garcia Marcelo H 2008 *Sedimentation Engineering*; ASCE.

Hyungsuk Kim, Kimura Ichiro and Shimizu Yasuyuki 2011 Numerical simulation of channel meandering processes; River, Coastal and Estuarine Morphodynamics: RCEM2011.

Hasegawa K 1981 Bank-erosion discharge based on a non-equilibrium theory; *Proc. JSCE, Tokyo* **316** 37–50 (in Japanese).

Ikeda S, Parker G and Sawai K 1981 Bend theory of river meanders: 1. Linear development; *J. Fluid Mech.* **112** 363–377.

Ikeda S, Yamasaka M and Chiyoda M 1987 Bed topography and sorting in bends; *J. Hydraul. Div.* **113** 190–206.

Johannesson H and Parker G 1989 Linear theory of river meanders; *Water Resour. Monograph.* **12** 181–213.

Julien P Y and Anthony D J 2002 Bed load motion and grain sorting in a meandering stream; *J. Hydraul. Res.* **40(2)** 125–133.

Kassem Ahmed and Chaudhry M H 2005 Effect of bed armoring on bed topography of channel bends; *J. Hydraul. Eng.* **131** 1136–1140.

Knighton David 1984 *Fluvial Forms and Processes*; John Wiley&Sons Inc., New York.

Kalkwijk J P T and de Vriend H J 1980 Computation of the flow in shallow river bends; *J. Hydraul. Res.* **18(6)** 327–342.

Koch F G and Flokstra C 1981 Bed level computations for curved alluvial channels; Proceedings of the XIXth Congress of the IAHR, pp. 357–364.

Kovacs A and Parker G 1994 A new vectorial bedload formulation and its application to the time evolution of straight river channels; *J. Fluid Mech.* **267** 153–183.

Karim F M and Holly F M Jr 1986 Armoring and sorting simulation in alluvial rivers; *J. Hydraul. Eng.* **112(10)** 705–715.

Lien H C, Hsieh T Y, Yang J C and Yeh K C 1999 Bend flow simulation using 2D depth-averaged model; *J. Hydraul. Eng.* **125(10)** 1097–1108.

Mosselman E 1998 Morphological modeling of rivers with erodible banks; *Hydrol. Process.* **12(10)** 1357–1370.

Nicholas A P and Smith G H S 1999 Numerical simulation of three-dimensional flow hydraulics in a braided channel; *Hydrol. Process.* **13** 913–929.

Odgaard A J 1981 Transverse bed slope in alluvial channel bends; *J. Hydraul. Div.* **107** 1677–1694.

Osman A M and Thorne C R 1988 Riverbank stability analysis. I: Theory; *J. Hydraul. Eng.* **114(2)** 134–150.

Schuurman F, Marra W A and Kleinhans M G 2013 Physics-based modeling of large braided sand-bed rivers: Bar pattern formation, dynamics and sensitivity; *J. Geophys. Res.: Earth Surface* **118(6)** 2509–2527.

Schumm Stanley A, Mpsley M Paul and Weaver William E 1987 *Experimental Fluvial Geomorphology*; New York, ISBN-10:0471830771.

Talmon A M, Struiksma N and Van Mierlo M C L M 1995 Laboratory measurements of the direction of sediment transport on transverse alluvial-bed slopes; *J. Hydraul. Res.* **33** 4.

Varshney D V 1975 Shear distribution in bend in rectangular channels; *J. Hydraul. Div., ASCE* **101(10)** 1053–1066.

Van Rijn L C 1989 Sediment Transport by Currents and Waves; Report H461, Technical Report, Delft Hydraulics.

Van Rijn L C 1993 *Principles of sediment transport in rivers, estuaries and coastal seas*; Aqua Publications, The Netherlands.

Van Dijk W M, van de Lageweg W I and Kleinhans M G 2012 Experimental meandering river with chute cut-offs; *J. Geophys. Res.* **117** F03023.

Wang H, Zhou G and Shao X J 2010a Numerical simulation of channel pattern changes. Part I: Mathematical model; *Int. J. Sedim. Res.* **4** 366–378.

Xia J Q, Wang G Q and Wu B S 2003 Numerical simulation for the longitudinal and lateral deformation of riverbed in the lower Yellow River. 1: Establishment of a 2-D composite model. Numerical simulation of flow and bed deformation in meandering rivers considering the erosion of bank; *Adv. Water Sci.* **14(6)** 390–395.

Yen C L and Lee K T 1995 Bed topography and sediment sorting in channel bend with unsteady flow; *J. Hydraul. Eng.* **121(10)** 591–599.

Zimmerman C and Kennedy J F 1978 Transverse bed slopes in curved alluvial streams; *J. Hydraul. Div.* **104** 33–48.

Zolezzi G and Seminara G 2001 Downstream and upstream influence in river meandering. Part1: General theory and application to overdeepening; *J. Fluid Mech.* **438** 183–211.

MS received 3 July 2015; revised 1 October 2015; accepted 15 October 2015